Metals & corrosion

Cu–Ag and Ni–Ag meshes based on cracked template as efficient transparent electromagnetic shielding coating with excellent mechanical performance

A. S. Voronin[1,2,*] , Y. V. Fadeev[1], I. V. Govorun[3,4], I. V. Podshivalov[3], M. M. Simunin[1,2,4], I. A. Tambasov[3], D. V. Karpova[1], T. E. Smolyarova[2,3], A. V. Lukyanenko[2,3], A. A. Karacharov[5], I. V. Nemtsev[1,2,3], and S. V. Khartov[1]

[1] Federal Research Center «Krasnoyarsk Science Center, Siberian Branch, Russian Academy of Sciences» (FRC KSC SB RAS), Krasnoyarsk, Russia 660036

[2] Siberian Federal University, Krasnoyarsk, Russia 660041

[3] Kirensky Institute of Physics, Siberian Branch, Russian Academy of Sciences, Krasnoyarsk, Russia 660036

[4] Reshetnev Siberian State University of Science and Technology (Reshetnev University), Krasnoyarsk, Russia 660037

[5] Institute of Chemistry and Chemical Technology, Siberian Branch, Russian Academy of Sciences, Krasnoyarsk, Russia 660036

ABSTRACT

Nowadays, the technical advances call for efficient electromagnetic interference (EMI) shielding of transparent devices which may be subject to data theft. We developed Cu–Ag and Ni–Ag meshes on flexible PET substrate for highly efficiency transparent EMI shielding coating. Cu–Ag and Ni–Ag meshes obtained with galvanic deposition of copper and nickel on thin Ag seed mesh which was made by cracked template method. Coefficients S_{11}, S_{21} and shielding efficiency (*SE*) were measured for Cu–Ag and Ni–Ag meshes in X-band (8–12 GHz) and K-band (18–26.5 GHz). 90 s copper deposition increase *SE* from 23.2 to 43.7 dB at 8 GHz with a transparency of 82.2% and a sheet resistance of 0.25 Ω/sq. The achieved maximum *SE* was 47.6 dB for Cu–Ag mesh with 67.8% transparency and 41.1 dB for Ni–Ag mesh with 77.8% transparency. Cu–Ag and Ni–Ag meshes have high bending and long-term stability. Minimum bend radius is lower than 100 μm. This effect allows to produce different forms of transparent shielding objects, for example, origami method. Our coatings are the leading among all literary solutions in three-dimensional coordinates: of sheet resistance–optical transmittance–cost of produced.

Springer

GRAPHICAL ABSTRACT
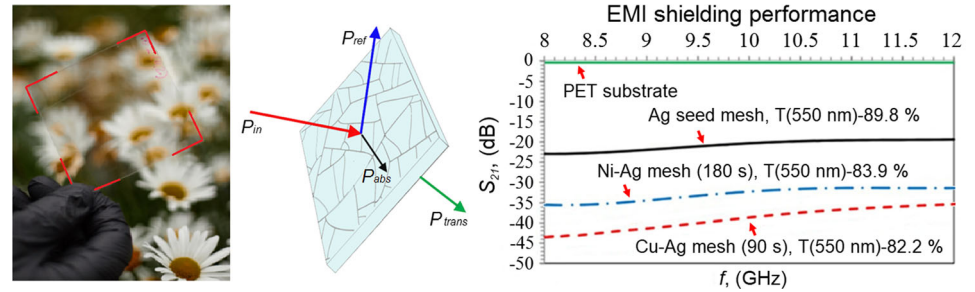
Introduction

Transparent conductive coating (TCC) should have a shielding efficiency (*SE*) of long-wave radiation of at least 30–40 dB. This corresponds to a decrease in the intensity of incident radiation by 10^3–10^4 times or shielding 99.9–99.99% of power, with the maximum possible transparency in the visible range. Metal micro- and nanostructures are the most likely for EMI shielding because of their low sheet resistance and high optical transmittance [1].

The first type of transparent conductive coating which are perspective at EMI shielding application is nanoconductor thin film, for example Ag [2–4] and Cu [5] nanowires (NW), Ag [6] and Cu [7] nanofibers (NF) obtained by electrospinning method. It's important to tell about the following researches as effective EMI shielding coatings. Composite CA (calcium alginate)/AgNW/PU [2] with optical transmittance 81 % has *SE* value 31.3 dB at 8–12GHz. AgNW thin film on PDMS substrate [3] with optical transmittance 85.2% has *SE* value ∼ 38 dB at the same range. Metal NW films have shielding efficiency that exceed the characteristics of nonmetallic transparent conductive coating, e.g., transparent conductive oxides—AZO [8], single walled carbon nanotube (SWCNT) [9], graphene monolayer [10], graphene/PMMA heterostructures (3 layer) [11], conductive polymers—PANI [12], PEDOT:PSS [13]. The features of NW coating include a strong decrease in transparency and an increase haze up to 10% [14] during the formation of films with a sheet resistance less than 10 Ω/sq.

Mechanical properties of Ag NW [15] or Cu NW [16] films as well as NW meshes produced by laser welding technique [17] are characterized by high bending resistance, i.e., more than 10^5 cycles at a small bending radius of 1 mm and less [15, 17]. Degradation in bending with a small radius in this class of coatings is associated with the breakdown of contact between single NW films, and in the case of welded NW films, degradation is associated with plastic deformation of NW accompanied by their destruction. Films based on pure Ag and Cu NW are characterized by low chemical stability in atmospheric air and humidity due to oxidation, in the case of Ag NW [18] oxidation is due to sulfur-containing substances (H_2S, etc.), for Cu NW [16] oxidation associated with atmospheric oxygen and water vapor. The problem of the long-term chemical stability of NW films is solved by graphene monolayer [19], or by depositing a protective layer, for example, Ni, Au [20], or a polymer layer [21, 22].

The second type of transparent conductive coating is micro- and nanomeshes obtained by vacuum deposition of Ag, Cu and Au on lithographic templates. Templates can be made by photolithography [23–25], imprint lithography [26, 27], etc. Those coatings have a sheet resistance 3–20 Ω/sq with a transparency more than 75–95%, depending on the geometric characteristics of the template structure. Low sheet resistance and high optical transmittance make micro- and nanomeshes the most perspective materials for EMI shielding application. As example: thick square copper mesh has *SE* 38–42 dB at 8–12 GHz [28]. Control of geometrical parameters of micro- and nanomeshes is effective for optical properties optimization. Thus, micromeshes with a more complex geometry were considered, for example, a petal-shaped mesh with a transparency 73.4% is characterized by *SE* ∼ 32.1 dB at 12.2 GHz [29]. In [30], a rotating circle mesh with a transparency of

95% and characterized by a *SE* in the K-band (12–18 GHz) of 17–21 dB [30] was proposed.

The mechanical properties of metallic micro- and nanomeshes are similar to NW films, but they have different mechanisms of destruction. Metallic micro- and nanomeshes degrade under bending deformation of a small radius due to the development of cracks in the mesh; this mechanism is due to the plastic deformation of the mesh material having strong adhesion to the substrate. Metal meshes demonstrate high resistance to bending with a radius of up to 1–5 mm for at least $5 \cdot 10^4$ cycles [27]. Resistance to oxidation by water vapor, atmospheric oxygen, and sulfur-containing compounds under atmospheric conditions is significantly higher than that of NW films, due to the absence of contact resistances between individual elements.

Metal meshes obtained using self-organization processes have a low sheet resistance, and therefore high *SE*, high resistance to bending deformation and long-term stability and also have a low production cost. The following approaches based on the self-organization process can be emphasized: cracked template [31–34], emulsion lithography [35], grain boundary lithography [36], microsphere lithography [37, 38].

Cracked template based on micromesh has the high figure of merit, scalability and low production cost by basic fundamental natural process—dehydration self-organization. In [39], there are prospects of using micromesh structures obtained by Ag vacuum deposition on a cracked template in the EMI shielding problem. So Ag mesh based on cracked template with a transparency 91% characterized by *SE* of 26 dB at 12 GHz. Mechanical properties of micromeshes based on cracked template are comparable to metallic micro- and nanomeshes obtained by standard lithography methods.

Our work is a logical continuation of the studies [39] already carried out and is aimed at increasing the efficiency of shielding by reducing the sheet resistance of micromesh by galvanic deposition of copper and nickel.

The technological process of Cu–Ag and Ni–Ag meshes formation proposed in the work is shown in Fig. 1

Experimental procedures

Materials

Egg white and yolk were taken from eggs (OJSC Poultry Farm Barkhotovskaya, the highest category) bought at the food market. Nickel chloride heptahydrate ($NiCl_2 \cdot 6H_2O$), nickel sulfate ($NiSO_4 \cdot 7H_2O$); copper sulfate pentahydrate ($CuSO_4 \cdot 5H_2O$), sulfuric acid (H_2SO_4), ethanol (C_2H_5OH), boric acid (H_3BO_3), saccharine—all chemical reagents were obtained from ChemReactivSnab (Russia). Ag target (99.99%) Kurt J. Lesker (USA). PET film with the thickness 50 μm was bought from HiFi Industrial Film Ltd (Japan).

Cracked template preparation

The egg white precursor for the cracked template was prepared according to the following procedure: in a fresh chicken egg, the white was separated from the yolk, then the white was thrown onto a coarse sieve with a mesh period of 500 μm. On a sieve, the egg white was separated into two fractions, the fluid mobile fraction flowed into the glass, and the viscous jelly-like fraction remained on the sieve. For the experiments we used a fluid fraction of egg white, to which we added egg yolk with a concentration of 3 ml/l.

To increase the adhesion of cracked films to the PET surface, the substrates were treated with oxygen plasma. The treatment was carried out on the Shungit magnetron sputtering system (the system was created on the basis of the Caroline D15 unit, ESTO-Vacuum LLC). The processing was carried out at a pressure of $\sim 2 \cdot 10^{-2}$ Pa, the beam power was $6.2 \cdot 10^{-2}$ kW, the processing time was 15 s. An example of cracked templates before and after oxygen plasma treatment is shown in Fig. S1 and S1b

Then the egg white precursor was deposited by the Meyer rod method on PET substrates. The thickness of the egg white precursor film is 30.48 μm (Meyer rod #12), which was deposited at a speed of 30 mm/s. After deposition, the liquid film was dried at room temperature ~ 21 °C and a humidity of 50%. Scanning electron microscopy (SEM) image of cracked template is shown in Fig. S1c.
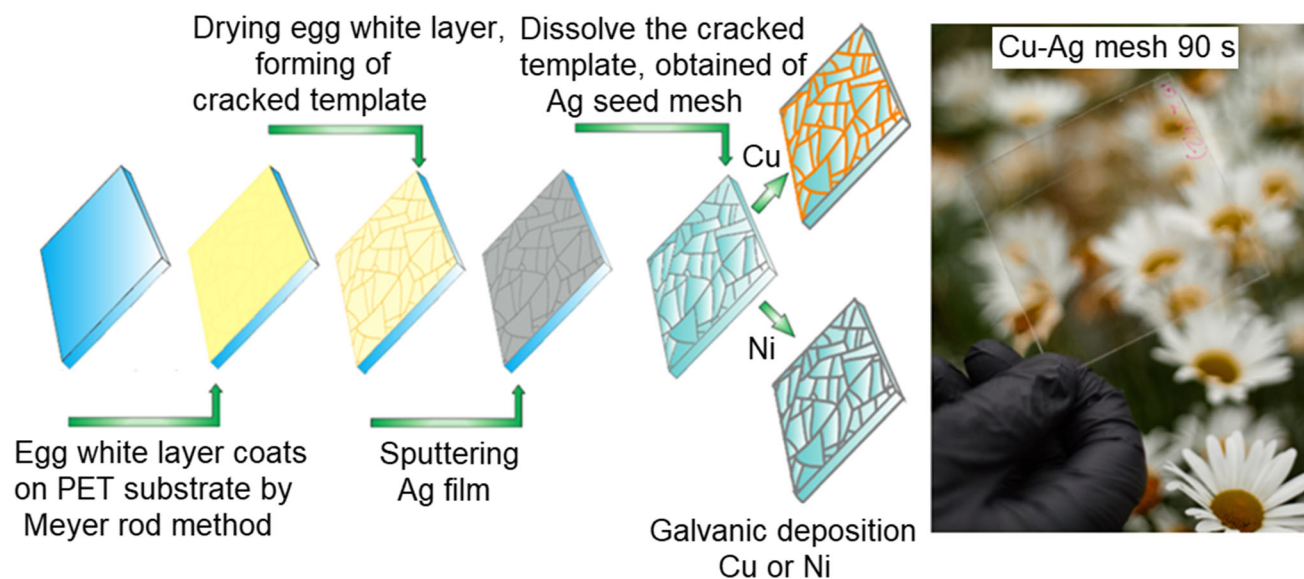
Figure 1 Technological scheme of the highly conductive Cu–Ag and Ni–Ag meshes formation.

Vacuum deposition Ag layer and obtained Ag seed mesh with contact pad

The magnetron sputtering of Ag seed mesh was carried out at the Emitech K575XD (Quorum Technologies Ltd, UK). The sputtering was made at the following parameters: current 40 mA, cycle duration 45 s, number of cycles 5, the thickness of the Ag film on a flat glass substrate was ∼ 200 nm. The contact pad for galvanic deposition was formed in the same deposition mode with masking 90% of the sample area.

Galvanic deposition of copper and nickel on Ag seed mesh

The galvanic deposition of Cu and Ni was carried out in a potentiostatic mode; the operating voltage was 0.5 V. The mass transfer of metals to the Ag seed mesh was controlled by the deposition time. In the work the following parameters of time of deposition: 15, 30, 90, 180, and 300 s were chosen.

As working electrolytes were used: copper electrolyte on 100 g of water: 25 g $CuSO_4 \cdot 5H_2O$; 5 g H_2SO_4; 0.0125 g NaCl; 5 g C_2H_5OH; nickel electrolyte on 100 g of water: 21 g $NiSO_4 \cdot 7H_2O$; 6 g $NiCl_2 \cdot 6H_2O$; 3 g H_3BO_3; 0.5 g saccharine. The reduction in copper and nickel at the cathode proceeds according to the following equations [40]

$$Cu^{2+} + 2\overline{e} \rightarrow Cu^0$$
$$Ni^{2+} + 2\overline{e} \rightarrow Ni^0 \qquad (1)$$

In an aqueous solution, relative to the standard hydrogen electrode, Cu^{2+} ions have an electrode potential of + 0.34 V, and Ni^{2+} ions have − 0.24 V. These metals are easily reduced at the cathode, because their potential is more than the potential of the water reduction reaction equal to − 0.41 V [40]. After galvanic deposition of Cu and Ni, the coatings were washed with deionized water and dried in air at a temperature of 80 °C.

Cu–Ag and Ni–Ag meshes characterization

The morphology of the crack templates and different mesh type was studied by the method of scanning electron microscopy (SEM) using HitachiTM3000 (Japan), with the accelerating voltage 15 kV. SEM equipped with an energy-dispersive X-Ray spectrometer XFlash 430 (EDX, Bruker, Germany).

The local surface morphology and thickness of meshes were determined by atomic force microscopy (AFM), DPN 5000 NanoInk (USA). For best results, scanning was carried out in semicontact mode using high-resolution cantilevers VIT_P/ IR (TipsNano) with a curvature radius of 10 nm.

The spectral dependencies of the optical transmittance of the meshes were measured in the range of 400–700 nm with a spectrophotometer Shimadzu UV-3600 (Japan). *I-U* characteristic were measured by the

two-electrode method using the IPPP-1 (Belarus). The measuring voltage range was − 50 mV to 50 mV. The sheet resistance of the mesh coatings was calculated according to the formula $R_s = tg\alpha_{I-U}L/W$, where α_{I-U}—the angle of slope of I-U characteristic, L—the distance between the contacts, W—the width of the contacts. In our case, the width of the contacts and the distance between them was 3 cm; as a result, the sheet resistance was equal to the tangent of the angle of slope I-U characteristic $R_s = tg\alpha_{I-U}$.

The mechanical properties of mesh coatings were studied in comparative experiments at laboratory stands. The main methods for testing mechanical properties include single and cyclic bending. The one time bending technique allows one to determine the effect of the bending radius on the sheet resistance of the mesh coatings. In our experiments, single bending radius varied from 50 mm to 100 μm. Cyclic bending allows you to explore the accumulation of fatigue in meshes. In our experiments, the number of bending cycles with a radius of 5 mm was 1000.

The long-term stability of Cu–Ag and Ni–Ag meshes to external conditions was studied in two modes. The first mode is a monthly exposure of Cu–Ag and Ni–Ag meshes at 100% humidity and room temperature, which was 21 °C. The second mode is a weekly exposure Cu–Ag and Ni–Ag meshes at a temperature of 85 °C and a humidity of 100%. The experimental procedure was as follows: a small container with distilled water was placed in a glass with a ground-in lid to maintain 100% humidity. Then the test sample was placed in the container and autoclaved according to the above test protocols. The value of the sheet resistance of the coating was used as an evaluation criterion.

The measurements of the contact angle of wetting, as a measure of the hydrophilic–hydrophobic properties of the meshes, were carried out by the "sessile" drop method. The measurements were carried out using an OCA 15EC automated optical analyzer equipped with a dosing device and a TDC-160 temperature sensor (DataPhysics, Germany). The volume of drops of deionized water in all experiments was fixed and equal to 5 μl, the dosing rate was 2 μl/s. In order to minimize distortions introduced into the value of the contact angle by the inhomogeneity of the surface of the meshes, measurements were made at least at three independent points of each coating, and then their values were averaged. The droplet

profile images obtained using the integrated camera were analyzed using the SCA software package (Version 5.0.12 Build 5012).

Shielding measurements

Electromagnetic reflected and transmitted scattering parameters (S_{11}, S_{21}) were measured using waveguide measurements Vector Network Analyzer (VNA) R&S ZVA 50 (Germany) (see appendix A Fig S2). The study was held in the X-band (8-12 GHz) and K-band (18-26.5 GHz), because these ranges are often studied as the characteristics of shielding materials. The samples under study were rectangular in shape. Their overall dimensions were chosen so that they completely overlap the waveguide window for both the X-band (23x10 mm) and the K-band (11x5.5 mm). To measure the reflection coefficient S_{11} and transmission coefficient S_{21} full two port calibration was performed.

Results and discussion

Morphology study and elemental analysis

A morphological study of the cracked template is given in many works, in particular, the morphology of the cracked template based on inorganic oxide sols SiO_2 [32, 41], TiO_2 [31, 42], as well as based on colloidal solutions containing polymer particles [39, 42] is considered. Egg white seems to be an optimal precursor for cracked template formation due to a combination of parameters: good adhesion to polymer and glass substrates, homogeneous cracking structure with no blind cracks and water solubility. SEM image (Fig. S1) shows a high quality cracked template based on egg white.

A SEM image of an Ag seed mesh is shown in Fig. 2a. An average path width of ∼ 4.7 μm and a fill factor of metal (FF), which is 9.8%, were determined using statistical analysis. The galvanic deposition of Cu and Ni leads to the fact that the mesh grows in width and height, which increases the FF in proportion to the deposition time. Cu–Ag and Ni–Ag meshes after 300 s of galvanic deposition are shown in Fig. 2b and Fig. 2c.

AFM images and profiles are presented for the Ag seed mesh in Fig. 2d, for Cu–Ag mesh, at 180 s copper deposition, in Fig. 2e and for Ni–Ag mesh, with a
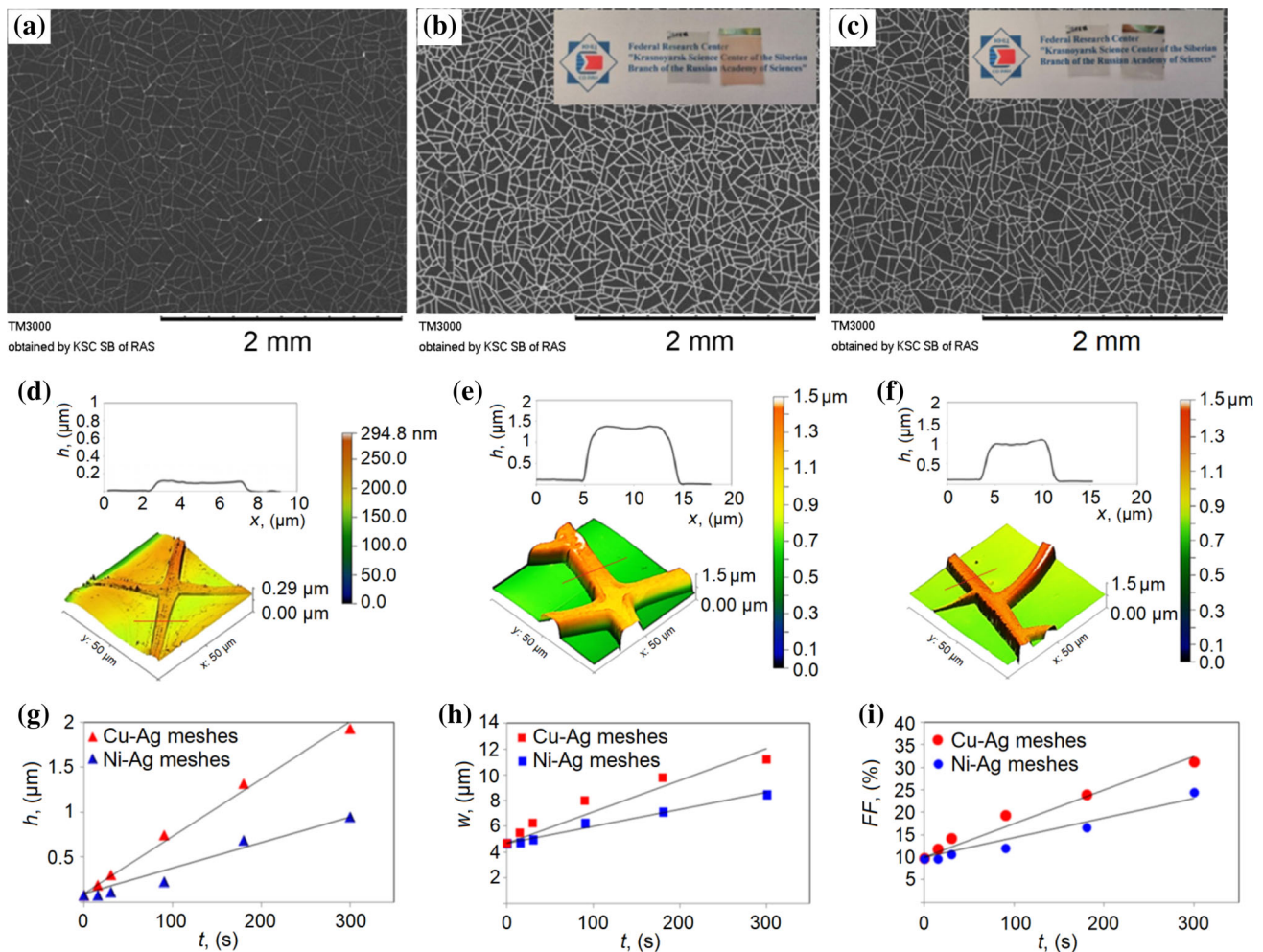
Figure 2 Scanning electron microscopy Ag seed mesh (**a**); galvanic Cu–Ag mesh after 300 s Cu deposition (**b**); Ni–Ag mesh after 300 s Ni deposition (**c**); AFM image and profile for Ag seed mesh (**d**) Cu–Ag mesh 180 s galvanic deposition (**e**) and Ni– galvanic deposition (**f**); dependence of the main geometric characteristics of Cu–Ag and Ni–Ag meshes, such as mesh thickness (**g**), mesh path width (**h**) and Fill Factor (**i**), on the time of galvanic deposition.

galvanic deposition time of 300 s, in Fig. 2f. The basic geometric parameters of the Cu–Ag and Ni–Ag mesh were determined depending on the time of the galvanic deposition of the metal using statistical processing of SEM and AFM images (Fig. 2g–i). The initial thickness of the Ag seed mesh is ∼ 109 nm (Fig. 2d), the coefficient of metal transfer to the bottom of the crack is approximately 0.515. Galvanic deposition of Cu over 300 s increases the thickness of the mesh to 1.92 μm. The dependence of the thickness on time is described by the linear law $h = 0.0063t + 0.1$, which corresponds to a deposition rate of 6.3 nm/s (Fig. 2g—red triangle). For Ni–Ag mesh, deposition increases the thickness to 0.95 μm in 300 s. The dependence of the thickness on time is described by the linear law $h = 0.0028t + 0.1$, which corresponds

to a deposition rate of 2.8 nm/s (Fig. 2g—blue triangle). The Ni–Ag mesh is characterized by internal stresses; therefore, an increase in thickness above 1 μm leads to peeling of the mesh from the substrate, and hence further deposition is impractical. Fig. 2h shows the dependence of the width of the path on the time of deposition of Cu or Ni. The width of the paths has a linear dependence on the deposition time, described by the following equations: $w = 0.0245t + 4.7$ (Fig. 2h—red square) for Cu–Ag mesh and $w = 0.0131t + 4.7$ for Ni–Ag mesh (Fig. 2h—blue square). Fill Factor, like other geometric parameters of the meshes, has a linear dependence on the time of galvanic deposition and described by the following equations: $FF = 0.0751t + 9.8$ (Fig. 2i—red circle) for Cu–Ag mesh and $FF = 0.0437t + 9.8$ (Fig. 2i—blue

circle) for Ni–Ag mesh. Thus, the rate of change of the Fill Factor can be estimated. For Cu–Ag mesh, it is 0.075%/s and for Ni–Ag mesh, 0.044%/s. Based on the obtained data, we can learn about the change in the optical transmission of Cu–Ag and Ni–Ag meshes at different galvanic deposition times, since T (%) $\sim$ 1-FF.

EDX analysis and SEM image of the back of Cu–Ag and Ni–Ag meshes with different deposition times are shown in Fig. 3. Between the Ag seed mesh and the deposited Cu and Ni there is a clear boundary without defects in the form of cavities (Fig. S3), which indicates good adhesion of the deposited metal to the Ag seed mesh. For the Cu–Ag mesh, three characteristic lines L_α, K_α, and K_β with energies of 0.928 keV, 8.046 keV, and 8.904 keV (Fig. 3c) were determined on the EDX spectrum. For Ni–Ag mesh, the L_α, K_α, and K_β lines with energies of 0.849 keV, 7.480 keV, and 8.267 keV (Fig. 3f) are observed [43].

There are also common lines on the EDX spectra—this is the L_α and L_β doublet with energies 2.983 keV and 3.15 keV, characteristic of the Ag seed mesh, and the oxygen lines ($K_\alpha \sim$ 0.525 keV) and carbon ($K_\alpha \sim$ 0.277 keV) related to the PET substrate.

Optoelectrical characterization Cu–Ag and Ni–Ag meshes

We can estimate optical transmission of the mesh by knowing its geometric parameters, according to the equation: $T = 1 - FF = \frac{(p-w)^2}{p^2}$ there p—the period of the mesh and w—the path width [44]. The optical transmission of the Ag seed mesh, as well as Cu–Ag and Ni–Ag meshes with different galvanic deposition times, are shown in Fig. 4a. The amount of optical transmittance is related to the FF. Mesh structure reflects the incident light, thereby creating a shadow proportional to FF. This explains the linear transmission for mesh structures in the visible range of 400–700 nm, as well as the near IR range (1200–4200 nm) [39].

The transparency of the Ag seed mesh at a wavelength of 550 nm is 89.8%, and according to Fig. 2i, the FF is $\sim$ 9.8%, which correlates well with the measured transmittance. The galvanic Cu and Ni deposition reduces the transparency of the meshes in proportion to the increase in FF for all of the coatings. For Cu–Ag meshes, we decided that coatings with a short deposition time of 15 s, 30 s, and 90 s are the most perspective. They have a transparency at a wavelength of 550 nm—87.5%, 85.4% and 82.2%. This conclusion is based on the high deposition rate. Cu–Ag mesh with a deposition time of 180 s and 300 s has
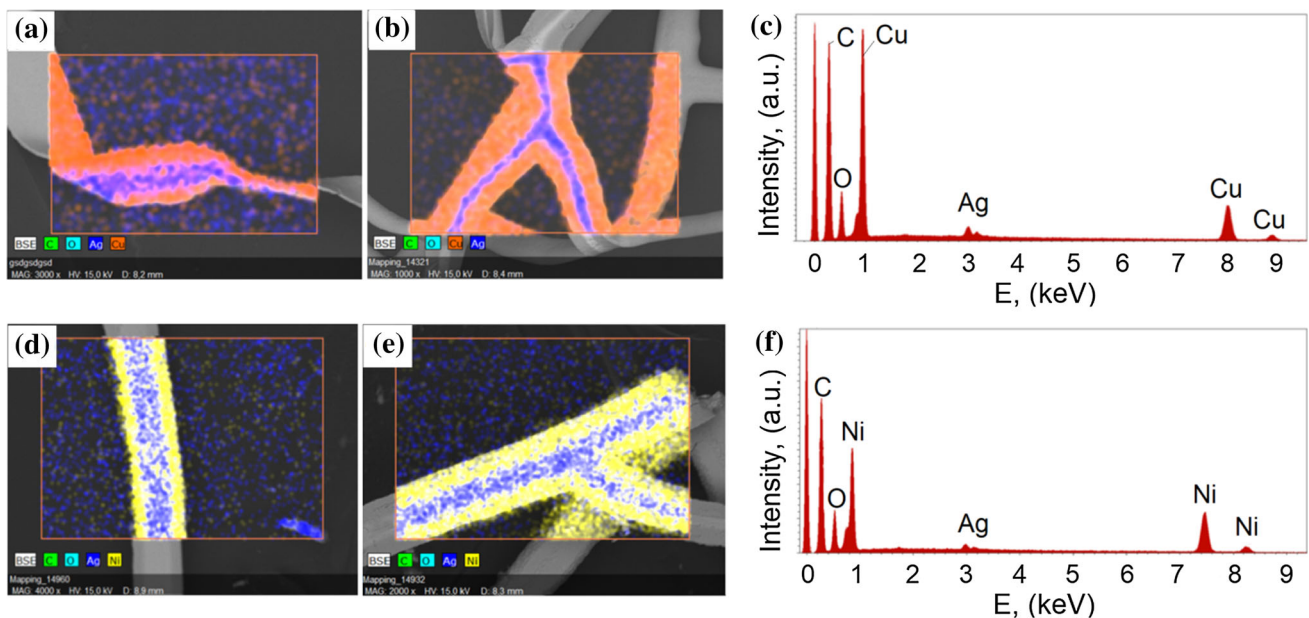

Figure 3 Elemental mapping Cu–Ag mesh 90 s (**a**) and 300 s (**b**) copper galvanic deposition and EDX spectra (**c**) elemental mapping Ni–Ag mesh 90 s (**d**) and 300 s (**e**) nickel galvanic deposition and EDX spectra (**f**).
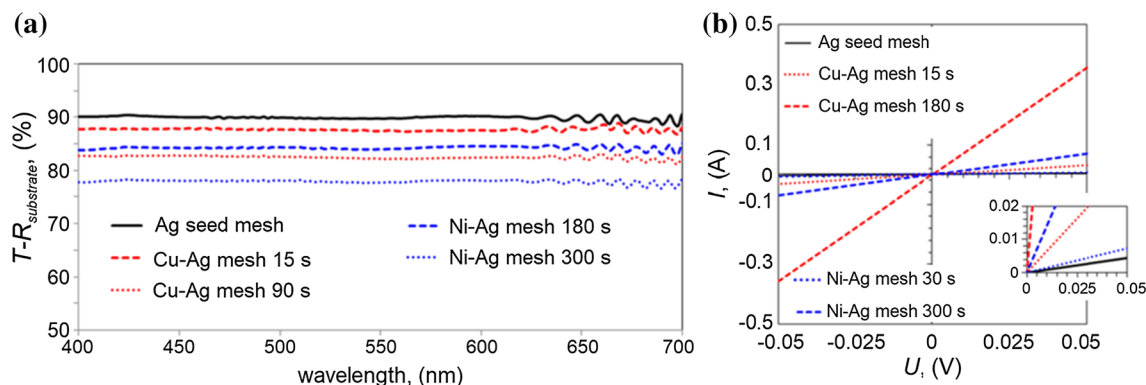
Figure 4 Transmittance spectra of Cu–Ag and Ni–Ag meshes with different deposition time (**a**); *I-U* characteristics for various Cu–Ag and Ni–Ag meshes (**b**).

a transmittance of 75.7% and 67.8% at a wavelength of 550 nm.

For Ni–Ag mesh, the deposition rate is lower; therefore, meshes with a deposition time of 90 s, 180 s and 300 s, which have a transparency at a wavelength of 550 nm—87.2 %, 83.9 % and 77.8 % can be noticed.

The linear behavior of the *I-U* characteristics, for all types of meshes (Fig. 4b), indicates the ohmic contact between the Cu–Ag and Ni–Ag mesh and silver contact pads. The selected voltage range from − 50 to 50 mV is dictated by the low sheet resistance of some meshes and the possible thermal degradation of PET substrates at currents more than 1.5 A. From the tangent of the slope of the *I-U* characteristics, the sheet resistance was calculated. For Ag seed mesh, it was ~11 Ω/sq. The sheet resistance for Cu–Ag meshes was 1.52, 0.62, 0.25, 0.14, and 0.06 Ω/sq for the entire sample of meshes. Ni–Ag meshes had a sheet resistance 9.3, 8.9, 3.8, 1.7 and 0.7 Ω/sq.

Figure of merit, determined by the ratio σ_{dc}/σ_{opt}, is a comparative integral characteristic of transparent electrodes of various type. The experimental points corresponding to the formed coatings in the coordinates sheet resistance-optical transmittance at 550 nm were approximated by the equation [38]

$$\frac{\sigma_{dc}}{\sigma_{opt}} = \frac{Z_0}{2R_s(T_{550nm}^{-1/2} - 1)} \qquad (2)$$

there *T*—the optical transmittance at a wavelength of 550 nm; R_s is the sheet resistance; $Z_0 = 377$ Ω is the vacuum impedance; the ratio σ_{dc}/σ_{opt} is the main integral characteristic of the transparent electrode.

Table 1 compares σ_{dc}/σ_{opt} for the entire sample of Cu–Ag and Ni–Ag meshes obtained in this work with the literature results.

The highest results of the σ_{dc}/σ_{opt} ratio were observed on the structures obtained by the cracked template method. Researchers are actively using an approach based on galvanic deposition of metal on seeds to obtain meshes with a high value of σ_{dc}/σ_{opt}, up to 30000 presented in [59].

Mechanical properties, long-term stability and wetting of galvanic Cu–Ag and Ni–Ag meshes

The mechanical properties of Cu–Ag and Ni–Ag meshes are substantially higher than fragile TCO, and close to highly flexible films of one-dimensional nanostructures. TCO is stable on flexible substrates under bending with a small radius of curvature [60, 61]. One-dimensional nanostructures such as SWCNT [62] metal nanowires [63] and metal nanotrough [64] are highly bendable and stretchable due to the movement of the individual structural elements of the coating relative to each other.

The bend test is directly a criterion that determines the flexibility of the coating under study. Bending stable depends on the material and thickness of the mesh, its adhesion to the substrate, as well as the thickness of the substrate. The thickness of the substrate determines the amount of displacement of the polymer macromolecules during bending, since the substrate experiences a tensile-compression deformation. Fig. 5a shows the dependence of the sheet resistance for Cu–Ag (left plot Fig.5a) and Ni–Ag (right plot Fig.5a) meshes on the value of the bending radius. The bending radius varied in the range of 100 μm–50 mm. There was no change in sheet resistance for the entire sample of coatings with a bend with a

Table 1 Optoelectrical parameters of different TCC

TCC	Method produced	T (550 nm), %	R_s, Ω/sq	σ_{dc}/σ_{opt}	References
ITO	Magnetron sputtering	85	19	117.2	[45]
ITO	Sol–gel deposition	88	110	28.5	[46]
SWCNT: Super acid doping	Vacuum filtration colloidal solution and transfer on PET substrate	90.9	60	64.3	[47]
SWCNT: HNO_3 doping	Aerosol filtration and transfer on PET substrate	90	110	31.6	[48]
SWCNT: $AuCl_3$ doping	Aerosol filtration and transfer on PET substrate	90	40	86.9	[49]
HNO_3 doped graphene	CVD and transfer graphene film on PET substrate	1 layer: 97.4	125	113.6	[50]
		4 layer: 90.1	∼ 30	117.4	
Ag nanowires	Meyer rod coating colloidal solution on substrate	∼ 85	10.3	215.4	[2]
	Vacuum filtration colloidal solution and transfer on PDMS substrate	85.2	3.1	730.6	[3]
	Meyer rod coating colloidal solution on PET substrate	∼ 92	5	884.9	[51]
Cu nanowires	Meyer rod coating colloidal solution on glass substrate	81	25	67.8	[52]
Ag mesh	Photolithography	80.2	8.2	197	[25]
Cu–Ni mesh	Imprint lithography	∼ 85	16.2	137.4	[53]
Ag mesh	Electrohydrodynamic jet printing	84.39	7	301.6	[54]
Mo mesh	Photolithography	97	30.2	383.9	[55]
Cu nanotrough network Au nanotrough network	Electrospun nanofibers template	90	2	1729.4	[56]
		94	7.5	788.7	
Au mesh	Grain boundary lithography	82.5	21	88.6	[36]
Ag NP mesh	Emulsion lithography	88	8.2	347.7	[57]
Au mesh	Cracked template	92	3.2	1386.1	[58]
Cu–Ag mesh	Cracked template	80	0.3	5385.7	[59]
		70	0.1	9617.3	
Cu–Ag mesh	Galvanic deposition Cu on seed mesh based on cracked template	15 s:87.5	1.52	1785.1	This work
		30 s:85.4	0.62	3646.1	
		90 s:82.2	0.25	7277.9	
		180 s:75.7	0.14	9019.1	
		300 s:67.8	0.06	14612.4	
Ni–Ag mesh	Galvanic deposition Ni on seed mesh based on cracked template	15 s:89.1	9.3	291.8	This work
		30 s:88.6	8.9	337.8	
		90 s:87.2	3.8	693.1	
		180 s:83.9	1.7	1200.6	
		300 s:77.8	0.7	2026.8	

radius of 5–50 mm. Firstly, this is due to the small thickness of the PET substrate and, secondly, to the plasticity of the metals of the meshes, which is sufficient to compensate for mechanical stresses in bending.

Bending with a radius of 100 μm is characterized by an irreversible change in the PET substrate associated with large local tension. Due to strong adhesion to the substrate, the metal mesh breaks due to the movement of polymer macromolecules relative to each other at small bending radius. With a small bending radius, the plasticity of metals in the mesh is not enough to compensate the deformation of the substrate. Ag seed mesh and Ni–Ag mesh, with
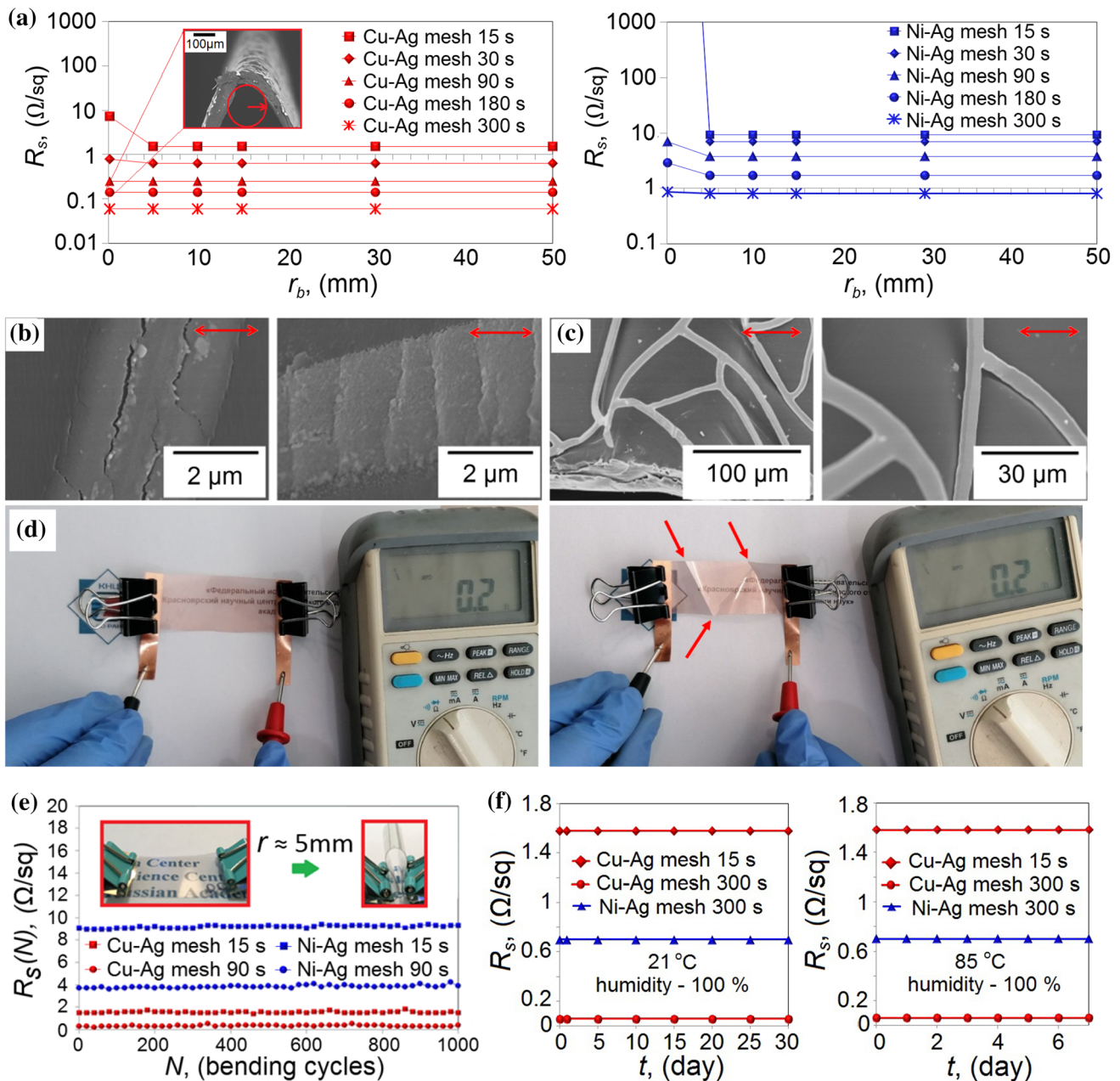
Figure 5 Dependence of the sheet resistance on the value of the single bend radius for Cu–Ag (left plot) and Ni–Ag meshes (right plot) (the insert shows a Cu–Ag mesh with 180 s galvanic deposition after bending with a radius of 100 μm in three places, irreversible changes in the substrate are visible) (**a**); SEM image of 30 s deposition Ni–Ag mesh morphology after bending with 100 μm radius (**b**), and SEM image of 180 s deposition Cu–Ag mesh morphology after bending with 100 μm radius (**c**); influence of origami-like bending on through resistance of Cu–Ag mesh with 300 s galvanic deposition (**d**); influence of cyclic bending with a radius of 5 mm on the sheet resistance of Cu–Ag and Ni–Ag meshes (**e**) (the insert shows a Ni–Ag mesh with 30 s galvanic deposition before and after bending with a radius of 5 mm); long-term stability of Cu–Ag and Ni–Ag meshes in various conditions: 1 month at 21 °C and 100% humidity (left plot), 1 week at 85 °C and 100% humidity (right plot) (**f**).

deposition times of 15 s and 30 s, behave the same during critical bending, breaking in the bending region (Fig.5b), and completely losing the through conductivity between the contact pads. An increase

in the thickness of the mesh increases the moment of force, as a result, at the point of tension, the mesh can peel off from the substrate (Fig.5c), which is an important factor in maintaining through conductivity

between the contact pads. Thus, meshes whose path thickness is bigger than 0.5 μm are able to peel off the substrate during bending with a radius of 100 μm; therefore, their sheet resistance does not change. These include Cu–Ag mesh with a deposition time of 90 s, 180 s and 300 s, as well as Ni–Ag mesh with a deposition time of 180 s and 300 s.

Also an important factor in stability to small bending radius is the geometry of the mesh. Mesh paths along to the direction of motion of the macromolecules of the substrate material are most often torn, as can be seen in the example of square and hexagonal meshes [65]. For cracked template assisted mesh, the value of mechanical stress is less due to their stochastic structure, because most of the paths are directed at an angle to the deformation vector.

For effective EMI shielding, the joint tightness is important, since they are most vulnerable to radiation leaks. Our Cu–Ag and Ni–Ag meshes can be folded using the origami method to give the film a complex geometry of the shielding object. Fig. 5d shows a Cu–Ag mesh with a deposition time of 300 s with three characteristic origami bends. As can be seen from Fig. 5d, these manipulations do not affect the sheet resistance of the Cu–Ag mesh.

Cyclic bending tests are also important for evaluating fatigue stresses in a Cu–Ag and Ni–Ag meshes. The effect of cyclic bending deformation with a radius of 5 mm for 1000 cycles on the absolute sheet resistance is shown in Fig. 5e. For Cu–Ag and Ni–Ag meshes with deposition times of 15 s and 90 s, there is no change in sheet resistance. Such an effect during cyclic bending deformation is characteristic of the entire sample of Cu–Ag and Ni–Ag meshes. All types of metal meshes, as well as metal nanowires and SWCNT films, have similar results in cyclic bending.

Long-term stability of Cu–Ag and Ni–Ag meshes is an important indicator and determines the possibility of using the offered coatings in practice in conditions of high humidity and wide temperature differences. The main degradation mechanism of this kind of coatings is the oxidation of the metal of the micromesh by atmospheric oxygen and water vapor. Fig. 5 f shows plots of the sheet resistance of Cu–Ag and Ni–Ag meshes at the month exposure at 100% humidity and room temperature 21 ° C (Fig. 5f left plot) and a week exposure at temperature of 85 °C and 100% humidity (Fig. 5f right plot). According to the results of observations, all considered Cu–Ag and Ni–Ag meshes are characterized by high chemical

stability to oxidation under the two described modes. This result can be explained by the high density of the deposited metal, which is confirmed by the data of SEM studies (Fig. S3), it is also worth noting that a similar result was observed in [66] for galvanic Cu mesh.

Table 2 provides a comparison of the mechanical performance and long-term stability of Cu–Ag and Ni–Ag meshes and literature results.

Table 2 shows that Cu–Ag and Ni–Ag meshes have mechanical parameters and long-term stability at elevated temperature and humidity comparable or superior to the most promising literature results in this field.

The wetting of heterogeneous coatings, which include Cu–Ag and Ni–Ag meshes, is an important characteristic of the surface. Wetting has significant practical importance for the formation of composite coatings with GO or rGO [70], PEDOT:PSS [71], solution methods, for example spin-coating.

Figure 6a shows a histogram of the change in the contact angle of the drop for Cu–Ag, Ni–Ag, and Ag seed meshes at the beginning of measurements and after the formation of the equilibrium profile.

The formation time of the equilibrium droplet profile grew with increasing roughness of the coating and lay in the range of 1–3 min. An increase in the time of galvanic deposition of Cu and Ni leads to a decrease in the hydrophilicity of the coatings due to an increase in surface roughness. For all types of Cu–Ag, Ni–Ag and Ag seed mesh, there is a transition from the classical wetting of a flat surface—the Young–Dupre mechanism observed on a PET substrate to the Wenzel wetting mechanism, which considers surface roughness. The initial PET substrate had a contact angle of 68.3 °. The contact angle for the Ag seed mesh was 68.9° (Fig. 6b), but already from the 15 s of galvanic deposition, a steady increase in the contact angle for Cu–Ag and Ni–Ag meshes was observed. An increase in the galvanic deposition time from 15 to 300 s contributes to an increase in the equilibrium contact angle from 69.3° to 90.1° (Fig. 6c) for the Cu–Ag mesh. For Ni–Ag mesh, the contact angle increases from 65.1 to 82.7 (Fig. 6d) in equilibrium state. The dynamics of the increase in the contact angle for Cu–Ag and Ni–Ag meshes is agree with the AFM results of the dependence of the thickness of meshes on the time of galvanic deposition of Cu and Ni.

Table 2 Summary of the mechanical performance and long-term stability of different TCC

TCC	Method formation	Type and thickness of substrate	Minimal bend radius, mm	Bending cycles and radius, ΔR lower than 10%	Long-term stability	Ref
PAA doping SWCNT	Meyer rod coating colloidal solution	PET/ -	5	10^6 at 5 mm	125 days at 85 °C and 85% (RH); Sheet resistance decreased	[67]
Welded SWCNT	Aerosol filtration and transfer on PET substrate	PET/ -	3	$2 \cdot 10^4$ at 5 mm	20 months at room conditions; ΔR lower than 10%	[68]
AuCl$_3$ doped graphene	CVD and transfer graphene on PET substrate	PET/ 100 μm	10	< 500 at 10 mm bend	21 days at room conditions; ΔR is 30%	[69]
Ag NW film	Spin-coating colloidal solution on PET substrate	PET/ 50 μm	0.2	1000 at 1.5 mm	–	[15]
Cu NW film	Meyer rod coating colloidal solution on PET substrate	PET/ 100 μm	2.5	1000 at 2.5 mm	42 days at room conditions; ΔR is 40%	[16]
Ag NW mesh	Selective laser sintering NW film	PET/ 100 μm	1	$3 \cdot 10^5$ at 1 mm	–	[17]
Cu nanotrough network	Electrospun nanofibers template	PET/ 178 μm	1	1000 at 1 mm bend	3 h at 70 °C and 70% (RH); ΔR is ~ 100%	[56]
Au nanotrough network	Electrospun nanofibers template	PET/ 178 μm	1	1000 at 1 mm bend	3 h at 70 °C and 70% (RH); ΔR lower than 10%	[56]
AgNi mesh	Imprint lithography	PES/ 200 μm	3	$5 \cdot 10^4$ at 5 mm	20 days at 85 °C and 85% (RH); ΔR is 289%	[27]
Ag NP mesh	Emulsion lithography	PET/ -	1	2000 at 1 mm	–	[57]
Cu mesh	Electroless deposition in cracked template	PET/ 80 μm	2	1000 at 4 mm bend	31 h at 130 °C; ΔR is 1000%	[32]
Cu–Ag mesh 90 s	Galvanic deposition Cu on seed mesh based on cracked template	PET/ 50 μm	0.1	1000 at 5 mm bend	ΔR is 0% for 30 days at 21 °C and 100% (RH); ΔR is 0% for 7 days at 85 °C and 100% (RH)	This work
Ni–Ag mesh 180 s	Galvanic deposition Ni on seed mesh based on crack template	PET/ 50 μm	0.1	1000 at 5 mm bend	ΔR is 0% for 30 days at 21 °C and 100% (RH); ΔR is 0% for 7 days at 85 °C and 100% (RH)	This work

The most important conclusion of the study of the wettability of Cu–Ag and Ni–Ag meshes is a decrease in hydrophilicity with an increase in the roughness of the mesh. It is important to notice these results in the formation of composite coatings with meshes and conductive SWCNT or rGO layers from aqueous suspensions, as well as protective coatings based on water-soluble polymers or GO.

EMI Shielding properties of Cu–Ag and Ni–Ag meshes

The shielding effectiveness of a material is defined as the ratio of incident power (P_i) to transmitted power (P_t). Therefore, for SE measured in decibels (dB) it is given by [72, 73]:
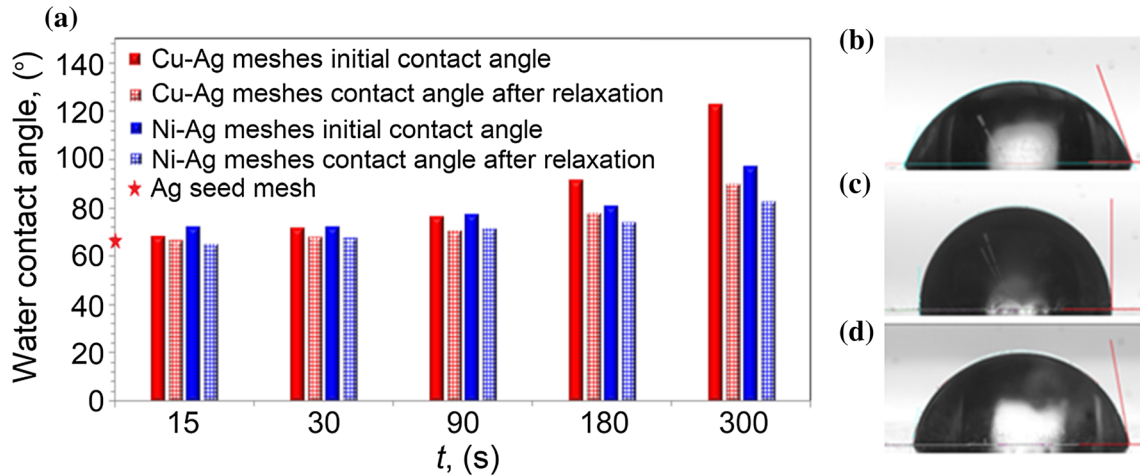
$$SE = 10 \lg \frac{P_i}{P_t} \tag{3}$$

Figure 6 Dependence of the contact angle of a drop in the initial state and after relaxation processes for Cu–Ag and Ni–Ag mesh depending on time (**a**); photograph of drops on Ag seed mesh (**b**) Cu–Ag mesh (**c**) and Ni–Ag mesh (**d**) after 300 s galvanic deposition.

Shielding of electromagnetic radiation occurs due to absorption and reflection [74]. The coefficients of transmission (T), reflection (R) and absorption (A) powers will be expressed as:

$$T = \frac{P_t}{P_i} = 10^{(0.1S_{21})} \tag{4}$$

$$R = \frac{P_r}{P_i} = 10^{(0.1S_{11})} \tag{5}$$

$$A = 1 - T - R \tag{6}$$

there P_r, P_t, P_i—power of reflected, transmitted and incident electromagnetic wave. Due to formula (4) SE can be expressed in decibels (dB):

$$SE = -10\lg T \tag{7}$$

The frequency dependences of the coefficient S_{21} for samples of Cu–Ag and Ni–Ag meshes in the X-band (8–12 GHz) and K-band (18–26.5 GHz) are shown in Fig. 7a and b.

In each of the frequency ranges, the dielectric PET substrate (Fig. 7a and b green line) and the Ag seed mesh (Fig. 7a and b black line) were measured. The S_{21} coefficient for the PET substrate is frequency independent in both the X-band and K-band. For PET substrates, the amount of power attenuation is negligible and amounts to 0.3 dB at 10 GHz. Application of an Ag seed mesh on a PET substrate with a thickness of ~109 nm leads to the fact that at a frequency of 10 GHz (the middle of X-band) the incident power decreases 100 times, which corresponds to a S_{21} value of −20 dB. Using formulas (4–6), we can estimate the part of the incident power that is

absorbed in the Ag seed mesh. In this case, about 20% is absorbed in the mesh, and 79% of the incident power is reflected from it. If we consider the K-band at 22 GHz, SE is 16 dB. In other words, only 2.5% of incident power passes through the Ag seed mesh.

As can be seen (Fig. 7a and b) for the Ag seed mesh, a weak dependence of the coefficient S_{21} on the frequency is observed. In the X-band, the power reduction smoothly decreases from −23.2 dB at a frequency of 8 GHz to −19.7 dB at a frequency of 12 GHz. Thus, the difference in the transmission level of the X-band boundary frequencies is 3.5 dB. If we consider the behavior of S_{21} in the K-band, we can see that the power level of the transmitted wave increases from -19.2 dB at a frequency of 18 GHz to −15.2 dB at a frequency of 26.5 GHz. The difference in S_{21} values at the K-band boundaries is 4 dB. It should be noted that the SE value for the Ag seed mesh correlates with the results of [75], where for Ag mesh based on cracked template 200 nm thick SE is observed equal to 25 dB at a frequency of 15 GHz.

During Cu or Ni deposition on Ag seed mesh, the plots shift to the region of lower S_{21} values, and the increase in the deposition time proportionally decreases the S_{21} value. This behavior is due to a decrease in the sheet resistance of Cu–Ag and Ni–Ag meshes. It is also worth noting that galvanic deposition increases the slope of the plots relative to the Ag seed mesh plot in the considering ranges (Fig. 7a and b).

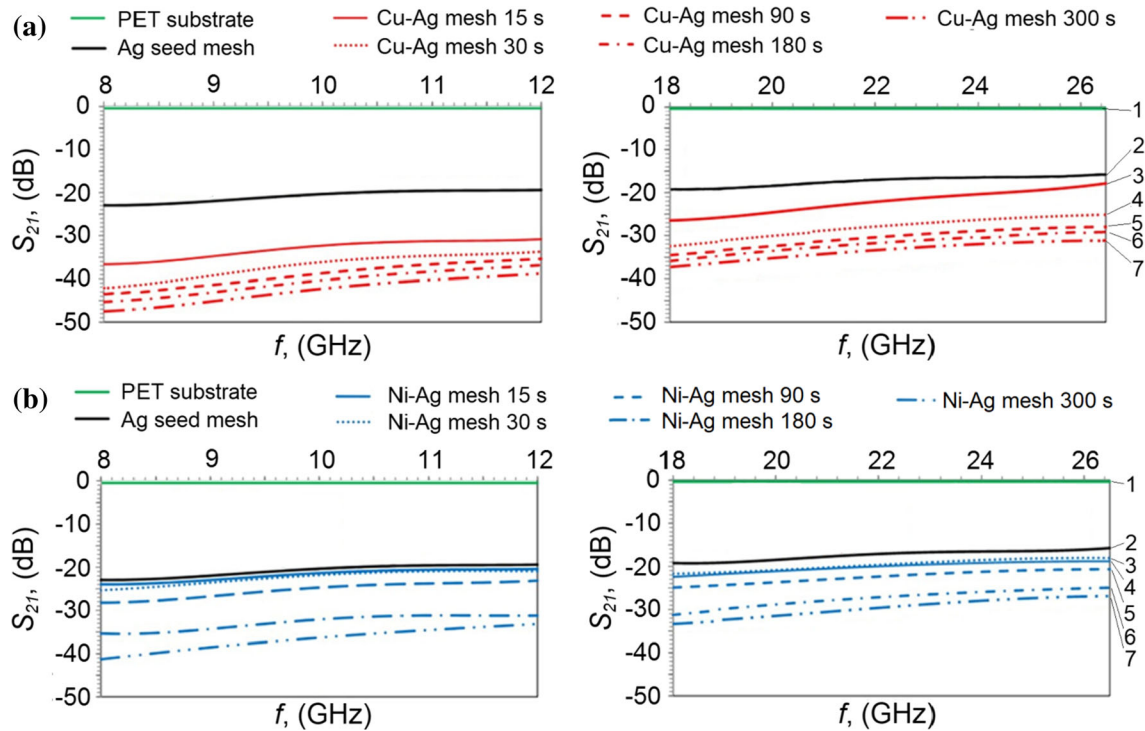The deposition of Cu on Ag seed mesh leads to a sequential shift in the plot of the coefficient S_{21},

Figure 7 Frequency dependence of the S_{21} parameter in the X-band and K-band for Cu–Ag (**a**) and Ni–Ag (**b**) meshes with different times of galvanic deposition.

reducing it to a minimum value of -47.6 dB at a frequency of 8 GHz for Cu–Ag mesh with a deposition time of 300 s (Fig. 7a). Ni deposition on an Ag seed mesh affects the S_{21} coefficient less than Cu. A Ni–Ag mesh with a deposition time of 300 s (Fig. 7b) has a minimum S_{21} value of -41.1 dB at 8 GHz. The lower S_{21} value for the Cu–Ag mesh is due to the lower sheet resistance relative to the Ni–Ag mesh.

Table 3 shows the values of the transmission coefficient S_{21} at the boundary frequencies of X- and K-bands for Cu–Ag and Ni–Ag meshes. Table 3 also shows the difference between the values of the transmission coefficient S_{21} at the boundaries of X- and K-bands, which characterizes the slope of the plots.

Table S1 shows the values of the transmission, reflection and absorption coefficients at the boundary frequencies of the X- and K-bands. Based on this table, we can conclude that the overwhelming part of the power is reflected from our coatings.

Figure 8 shows the dependences of SE for Cu–Ag and Ni–Ag meshes on galvanic deposition time. Graphics are plotted for different frequencies in the X-band (8–12 GHz) and K-band (18–26.5 GHz). To determine the SE value, the following procedures

were carried out: the S_{21} value was taken from the measured data at the required frequency and applied to formula (4), and then formula (7) was used. It should be noted that the case when the galvanic deposition time is 0 s corresponds to the Ag seed mesh.

The galvanic deposition of metal on an Ag seed mesh leads to an increase in the SE parameter, both for the case of Ag seed mesh with deposited Cu and for Ni too (see Fig. 8). In this case, the longer the deposition time, the stronger the SE of electromagnetic power. So the Cu–Ag mesh at a frequency of 10 GHz SE varies from 31.9 dB (power attenuation > 99.93%) to 42.3 dB (power attenuation > 99.99%) for a deposition time of 15 s and 300 s. Thus, the deposition of the Cu on the Ag seed mesh leads to the fact that SE increases by 11.9 dB at a deposition time of 15 s and by 22.3 dB at a deposition time of 300 s. When Ni is deposited on an Ag seed mesh, the SE values are lower, as noted earlier. So, at a frequency of 10 GHz with a deposition time of 15 s SE, it is 21.1 dB (power attenuation > 99.2%), and at 300 s SE it is 36.2 dB (power attenuation > 99.97%).

If we consider the K-band, it can be noted that SE behaves in a similar way, but the values of SE are

Table 3 Values of S_{21} coefficient for Cu–Ag and Ni–Ag meshes at the boundaries of the X- and K-band

TCC	S_{21}(8 GHz), dB	S_{21}(12 GHz), dB	S_{21}(18 GHz), dB	S_{21}(26.5 GHz), dB	$|S_{21}(8GHz)| - |S_{21}(12GHz)|$, dB	$|S_{21}(18GHz)| - |S_{21}(26.5GHz)|$, dB
Cu–Ag mesh 15 s	− 36.5	− 30.2	− 26.4	− 19.3	6.3	7.1
Cu–Ag mesh 30 s	− 42.4	− 32.8	− 32.5	− 26.7	9.6	5.8
Cu–Ag mesh 90 s	− 43.7	− 34.8	− 34.6	− 28.7	8.9	5.9
Cu–Ag mesh 180 s	− 45.4	− 36.2	− 36.1	− 30.5	9.2	5.6
Cu–Ag mesh 300 s	− 47.6	− 38.3	− 37.2	− 33.3	10.3	4.9
Ni–Ag mesh 15 s	− 23.8	− 19.9	− 21.3	− 17.8	3.9	3.1
Ni–Ag mesh 30 s	− 25.4	− 22.7	− 22.5	− 18.2	4.7	3.3
Ni–Ag mesh 90 s	− 28.5	− 23.7	− 24.3	− 20.7	4.8	3.6
Ni–Ag mesh 180 s	− 35.4	− 30.1	− 31.1	− 25.6	5	5.5
Ni–Ag mesh 300 s	− 41.1	− 33.4	− 33.1	− 28.1	7.7	5

lower than for the lower-frequency X-band. So, when Cu is deposited on an Ag seed mesh, SE increases by only 7 dB (from 16 dB to 23 dB) at 22 GHz for a deposition time of 15 s and by 20.2 dB (from 16 to 36.2 dB) at a deposition time of 300 s.

It is interesting to compare the mesh samples with similar sheet resistances, but with a different type of metal. Obviously, in this case, the SE should be the same. Consider a Cu–Ag mesh at a deposition time of 15 s, R_s= 1.52 Ω/sq (SE = 31.9 dB at a frequency of 10 GHz) and a Ni–Ag mesh at a deposition time of 180 s, R_s= 1.7 Ω/sq (SE = 31.6 dB at frequency 10 GHz). It can be stated that the SE values for the two samples are very close. In this case, as it should be, a lower value of R_s corresponds to a larger value of SE.

Let's compare mesh samples with similar optical transmittance values. Consider a Cu–Ag mesh with a deposition time of 15 s, T = 87.5%, R_s= 1.52 Ω/sq and SE = 36.5 dB at 8 GHz and a Ni–Ag mesh with a time of 90 s, T = 87.2%, R_s= 3.8 Ω/sq and SE = 28.5 dB at 8 GHz. It is noticeable that with almost the same optical transmittance, the copper-based mesh sample has a lower sheet resistance and, therefore, a large SE. Of course, this result is associated with a higher conductivity of Cu compared to Ni.

Thus, the efficiency of shielding the power of an electromagnetic wave depends on the sheet resistance R_s of the mesh. In this case, SE will increase with a decrease in R_s. Let's consider the mesh with the highest SE level. From Table 1 we can conclude that the Cu–Ag mesh sample with a deposition time of 300 s has the lowest sheet resistance among all the meshes studied in the work. For it R_s= 0.06 Ω/sq, SE is 47.6 dB at 8 GHz or power attenuation > 99.998% (Fig. 8).

It is necessary to analyze the studied samples of meshes by the combination of the following parameters: SE and optical transparency T. We are interested in mesh samples with a high level of optical transmittance (more than 75%) and with a significant SE level (at least 25 dB). This criterion includes: Cu–Ag meshes with the deposition time of 30 s, 90 s and 180 s having SE 42.4 dB, 43.7 dB and 45.4 dB at a frequency of 8 GHz, as well as 26.7 dB, 28.7 dB and 30.5 dB at a frequency of 26.5 GHz with optical transmittance of 85.4%, 82.2% and 75.7%, respectively. Ni–Ag mesh with a nickel deposition time of 180 s and 300 s, having SE 35.4 dB and 41.1 dB at a frequency of 8 GHz and 25.6 dB and 28.1 dB at a frequency of 26.5 GHz with an optical transparency
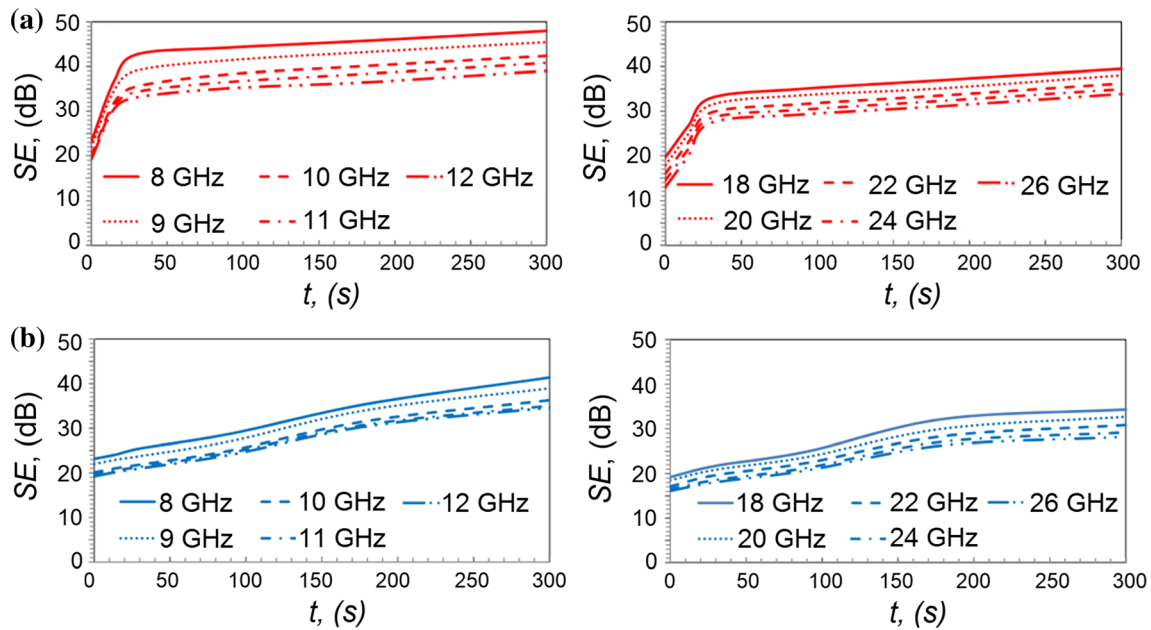
Figure 8 Dependence of the *SE* parameter on the time of galvanic deposition for Cu–Ag (**a**) and Ni–Ag (**b**) meshes in the X-band and K-band.

of 83.9% and 77.8%, respectively, are also suitable for these criteria.

The decrease in the S_{21} module and the *SE* with increasing frequency is associated with two factors: the frequency dependence of the sheet resistance and the perforated structure of the mesh coating.

The first factor is the frequency dependence of the sheet resistance of the metal of which the mesh is made. For conductors with a metallic type of conductivity, the active part of their sheet resistance increases with increasing frequency in proportion to the square root of the frequency. In [76] the formula describes the frequency dependence of the sheet resistance of a thin mesh coating $R^{mesh}(f)$. According to this article, this dependence can be represented as follows:

$$R^{mesh}(f) = \frac{1}{\sigma\delta(1 - e^{-h/\delta})}\frac{p}{2w} \tag{8}$$

$\delta = \sqrt{1/\pi f \mu \sigma}$ There σ—the direct current conductivity of the metal, h—the thickness of the mesh, p—mesh period, w—path width, δ—the depth of the skin layer, determined by the following expression:

Eq. (8) takes into account the geometry of the mesh coating. It should be noted that in the low-frequency limit (when the frequency tends to 0) and when the condition $p = 2w$ (the case of a continuous metal thin

film) is fulfilled, formula (8) goes over to the well-known equation [76]:$R(f \to 0) = 1/\sigma \cdot h$.

The second factor is the effect associated with the perforated structure of the mesh coating. Holes in metal screens cause radiation leakage due to the diffraction relationship between wavelength and hole size. According to [28], the *SE* value for a hole in a metal film is given by the following equation:

$$SE_{aperture} \approx 20\lg\frac{\lambda}{2d} \tag{9}$$

there d—is the linear size of the aperture, λ- is the radiation wavelength.

Our meshes are a stochastic lattice of holes in a Cu or Ni films. Simple estimates make it possible to determine the *SE* value for a single aperture in a metal screen. The average cell size for our Cu–Ag and Ni–Ag meshes is around 50 μm. Therefore, at the boundary frequencies of 8 GHz and 26.5 GHz, the wavelength is 3.75 cm and 1.13 cm. According to formula (9), the *SE* value for an aperture with a linear size of 50 μm decreases from 51.5 dB (at 8 GHz) to 41.1 (at 26.5 GHz). These estimates show that then the radiation wavelength is reduced, even microholes affect the *SE* value. Thus, we can conclude that for mesh coatings, two factors affect the frequency dependence, which give similar graph behavior.

As indicated above (see Figs. 7 and 8), *SE* depends on the sheet resistance value R_s. In [76], a formula is

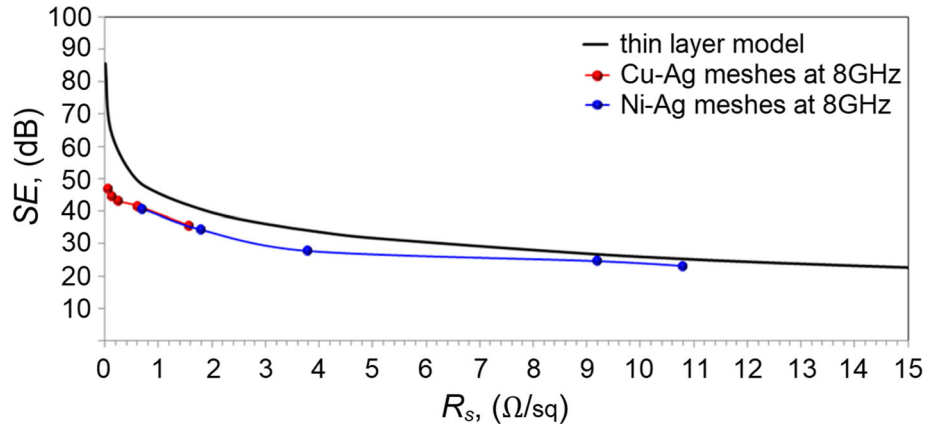**Figure 9** Dependence of *SE* on the sheet resistance R_s for the Cu–Ag and Ni–Ag meshes studied in the work.

Table 4 Comparison of the transparency parameters and *SE* for various TCC

TCC	Method produced	T (550 nm), %	f, GHz	SE, dB	References
AZO	Magnetron sputtering	85.46	1	13.1	[8]
AZO/Ag/TiO2	Magnetron sputtering	91.6	8	27.7	[77]
Graphene	CVD and transfer graphene on PET substrate	1L: 97.3	18		[78]
		4L: 89.6	18	10.01	
		8L: 80.5	18	19.14	
SWCNT film	Vacuum filtration colloidal solution and transfer on PET substrate	90	10	28	[9]
Ag NW	Vacuum filtration colloidal solution and transfer on PDMS substrate	85.2	8	38	[3]
Cu–Ag nanowires	Electroless plating Cu on Ag NW seed film	58	1–150	∼55	[79]
Ag mesh	Electrohydrodynamic jet printing	84.4	8	20.75	[54]
Ag NP mesh	Emulsion lithography	88	8	∼23	[57]
Ni–Ag galvanic mesh	Photolithography	85	8	∼40	[80]
Ag mesh	Cracked template	91	12	26	[39]
Cu–Ag galvanic mesh	Galvanic deposition Cu on seed mesh based on cracked template	85.4	8	42.4	This work
			12	32.8	
Ni–Ag galvanic mesh	Galvanic deposition Ni on seed mesh based on cracked template	83.9	8	35.4	This work

given that relates these two parameters in the framework of a thin layer model:

$$SE = 20 \lg \left(1 + \frac{Z_0}{2R_s}\right) \qquad (10)$$

there $Z_0 = 377\ \Omega$ is the wave impedance of free space.

The thin layer model well describes the experimental data for thin metal films, AZO [8], layered AZO/Ag/TiO$_2$ [77] structures, and Ag NW films [2, 3]. Their structure can be represented as continuous or quasi-continuous. For continuous and quasi-continuous coatings [2, 3, 8, 77], a weak frequency dependence of *SE* is observed. Meanwhile, for mesh coatings, there is a different behavior: the *SE* is significantly dependent on the frequency. For example, in [28, 30], *SE* decreases with the frequency increasing. This is also confirmed by the results obtained in this work (see Figs. 7, 8).

Figure 9 shows the dependence of *SE* on R_s using formula (10) and measured data. To calculate *SE*, a procedure similar to that used in the construction of Fig. 8. The calculation was performed at a frequency of 8 GHz.

It is seen (see Fig. 9) that the data obtained experimentally in this work (red and blue lines) qualitatively match with the thin layer model. The

maximum difference between the experimental data and the thin layer model can be observed in the region where the sheet resistance is less than 1 Ω/sq. Obviously, the *SE* values for the Cu–Ag and Ni–Ag meshes studied in this work will correlate well with the thin layer model in the lower frequency region, there the influence of the aperture effect is weaker. For example, in [28] it was shown that metal meshes at frequencies below 3 GHz demonstrate *SE* values that correlate well with the thin layer model. Also, the differences in the *SE* values for the thin layer model and Cu–Ag and Ni–Ag meshes are related to the fact that in formula (10), when calculating *SE*, the value of R_s measured at direct current is used. And, as mentioned above, sheet resistance grows with increasing frequency (see formula 8). All these factors lead to an increase in the power of the electromagnetic wave transmitted through the mesh coating, and, consequently, to a decrease in *SE*.

Table 4 shows a comparison of *SE* and optical transparency values at the boundary frequencies of the X-band and K-band ranges for various transparent conductive coatings.

From the analysis of Table 4, we can conclude that the Cu–Ag mesh samples proposed and studied in this work are *SE* superior then all film samples made using various techniques, such as TCO, carbon nanostructure, metal meshes obtained by vacuum deposition. Mesh coatings obtained by lithographic processes combined with the operation of galvanic deposition[80] have similar values of optical transparency and *SE*. It should be noted that the highest optical transparency ($\sim$ 91%) was demonstrated by the film samples made using the AZO/Ag/TiO$_2$ [77] and cracked template Ag mesh [39] technologies; however, the *SE* of these films is much lower than that of the Cu–Ag mesh.

Conclusion

In this work, highly conductive Cu–Ag and Ni–Ag meshes were obtained by galvanic deposition of Cu and Ni on a thin Ag seed mesh formed using a cracked template. Our meshes demonstrate high performance as transparent EMI shielding films. The Cu–Ag mesh with the characteristics *SE* = 42.4 dB at a frequency of 8 GHz and a transparency of 85.4% at 30 s of galvanic copper deposition and *SE* = 43.7 dB with a transparency of 82.2% at 90 s turned out to be the

most effective. The best *SE* result for Ni–Ag mesh is 35.4 dB and 83.9% transparency for 180 s galvanic deposition. The mechanical properties of the Cu–Ag and Ni–Ag mesh with a thickness more than 500 nm allow the formation of effective shielding objects of complex shape by the origami method, which eliminates the leakage of electromagnetic radiation at the junction of the two coatings. This fact opens up prospects for the practical application of our coatings.

Declarations

Conflict of interest   There are no conflicts to declare.

Supplementary Information: The online version contains supplementary material available at http s://doi.org/10.1007/s10853-021-06206-4.

References

[1] Guo CF, Ren ZF (2015) Flexible transparent conductors based on metal nanowire networks. Mater Today 18:143–154

[2] Jia LC, Yan DX, Liu XF, Ma RJ, Wu HY, Li ZM (2018) Highly efficient and reliable transparent electromagnetic interference shielding, film. ACS Appl Mater Interfaces 10:11941–11949

[3] Jung J, Lee H, Ha I, Cho H, Kim KK, Kwon J, Won P, Hong S, Ko SH (2017) Highly stretchable and transparent electromagnetic interference shielding film based on silver nanowire percolation network for wearable electronics applications. ACS Appl Mater Interfaces 9:44609–44616

[4] Hu MJ, Gao JF, Dong YC, Li K, Shan GC, Yang SL, Li RKY (2012) Flexible transparent PES/silver nanowires/PET sandwich-structured film for high-efficiency electromagnetic interference shielding. Langmuir 28:7101–7106

[5] Wang RL, Ruan HB (2016) Synthesis of copper nanowires and its application to flexible transparent electrode. J Alloy Compd 656:936–943

[6] Bai XP, Liao SY, Huang Y, Song JA, Liu ZL, Fang MH, Xu CC, Cui Y, Wu H (2017) Continuous draw spinning of extra-long silver submicron fibers with micrometer patterning capability. Nano Lett 17:1883–1891

[7] Wu H, Hu LB, Rowell MW, Kong DS, Cha JJ, McDonough JR, Zhu J, Yang YA, McGehee MD, Cui Y (2010) Electro-spun metal nanofiber webs as high-performance transparent electrode. Nano Lett 10:4242–4248

[8] Choi YJ, Kang KM, Lee HS, Park HH (2015) Electromagnetic interference shielding behaviors of Zn-based conducting oxide films prepared by atomic layer deposition. Thin Solid Films 583:226–232

[9] Xu H, Anlage SM, Hu LB, Gruner G (2007) Microwave shielding of transparent and conducting single-walled carbon nanotube films. Appl Phys Lett 90:183119

[10] Hong SK, Kim KY, Kim TY, Kim JH, Park SW, Kim JH, Cho BJ (2012) Electromagnetic interference shielding effectiveness of monolayer graphene. Nanotechnology 23:455704

[11] Zhang HL, Xia Y, Gai JG (2018) Ultrathin active layer for transparent electromagnetic shielding window. ACS Omega 3:2765–2772

[12] Kim BR, Lee HK, Kim E, Lee SH (2010) Intrinsic electromagnetic radiation shielding/absorbing characteristics of polyaniline-coated transparent thin films. Synth Met 160:1838–1842

[13] Xia YJ, Fang J, Li PC, Zhang BM, Yao HY, Chen JS, Ding J, Ouyang JY (2017) Solution-processed highly superparamagnetic and conductive PEDOT:PSS/Fe$_3$O$_4$ nanocomposite films with high transparency and high mechanical flexibility. ACS Appl Mater Interfaces 9:19001–19010

[14] Araki T, Jiu JT, Nogi M, Koga H, Nagao S, Sugahara T, Suganuma K (2014) Low haze transparent electrodes and highly conducting air dried films with ultra-long silver nanowires synthesized by one-step polyol method. Nano Res 7:236–245

[15] Song M, You DS, Lim K, Park S, Jung S, Kim CS, Kim DH, Kim DG, Kim JK, Park J, Kang YC, Heo J, Jin SH, Park JH, Kang JW (2013) Highly efficient and bendable organic solar cells with solution-processed silver nanowire electrodes. Adv Funct Mater 23:4177–4184

[16] Rathmell AR, Wiley BJ (2011) The synthesis and coating of long, thin copper nanowires to make flexible, transparent conducting films on plastic substrates. Adv Mater 23:4798–4803

[17] Kim SJ, Yoon HG, Kim SW (2021) Extremely robust and reliable transparent silver nanowire-mesh electrode with multifunctional optoelectronic performance through selective laser nanowelding for flexible smart devices. Adv Eng Mater 2001310

[18] Deignan G, Goldthorpe IA (2017) The dependence of silver nanowire stability on network composition and processing parameters. RSC Adv 7:35590–35597

[19] Deng B, Hsu PC, Chen GC, Chandrashekar BN, Liao L, Ayitimuda Z, Wu JX, Guo YF, Lin L, Zhou Y, Aisijiang M, Xie Q, Cui Y, Liu ZF, Peng HL (2015) Roll-to-Roll encapsulation of metal nanowires between graphene and plastic substrate for high-performance flexible transparent electrodes. Nano Lett 15:4206–4213

[20] Ye SR, Stewart IE, Chen ZF, Li B, Rathmell AR, Wiley BJ (2016) How copper nanowires grow and how to control their properties. Accounts Chem Res 49:442–451

[21] Choi JH, Lee KY, Kim SW (2019) Ultra-bendable and durable Graphene-Urethane composite/silver nanowire film for flexible transparent electrodes and electromagnetic-interference shielding. Composite Part B Eng 177:107406

[22] Miao L, Liu GJ, McEleney K, Wang JD (2019) Epoxy-embedded silver nanowire meshes for transparent flexible electrodes. J Mater Sci 54:10355–10370

[23] Lim JW, Lee YT, Pandey R, Yoo TH, Sang BI, Ju BK, Hwang DK, Choi WK (2014) Effect of geometric lattice design on optical/electrical properties of transparent silver grid for organic solar cells. Opt Express 22:26891–26899

[24] Ok JG, Kwak MK, Huard CM, Youn HS, Guo LJ (2013) Photo-roll lithography (PRL) for continuous and scalable patterning with application in flexible electronics. Adv Mater 25:6554–6561

[25] Qi LF, Li J, Zhu CT, Yang Y, Zhao SJ, Song WJ (2016) Realization of a flexible and mechanically robust Ag mesh transparent electrode and its application in a PDLC device. RSC Adv 6:13531–13536

[26] Kang MG, Guo LJ (2007) Nanoimprinted semitransparent metal electrodes and their application in organic light-emitting diodes. Adv Mater 19:1391–1396

[27] Kim HJ, Lee SH, Lee J, Lee ES, Choi JH, Jung JH, Jung JY, Choi DG (2014) High-durable AgNi nanomesh film for a transparent conducting electrode. Small 10:3767–3774

[28] Keith TJ, Matthew WP, Jennifer IH, Keith AR (2009) Predicted and measured EMI shielding effectiveness of a metallic mesh coating on a sapphire window over a broad frequency range Proc.SPIE:7302

[29] Wang WQ, Bai BF, Zhou Q, Ni K, Lin H (2018) Petal-shaped metallic mesh with high electromagnetic shielding efficiency and smoothed uniform diffraction. Opt Mater Express 8:3485–3493

[30] Wang HY, Lu ZG, Tan JB (2016) Generation of uniform diffraction pattern and high EMI shielding performance by

metallic mesh composed of ring and rotated sub-ring arrays. Opt Express 24:22989–23000

[31] Han B, Pei K, Huang YL, Zhang XJ, Rong QK, Lin QG, Guo YF, Sun TY, Guo CF, Carnahan D, Giersig M, Wang Y, Gao JW, Ren ZF, Kempa K (2014) Uniform self-forming metallic network as a high-performance transparent conductive electrode. Adv Mater 26:873–877

[32] Kiruthika S, Gupta R, Rao KDM, Chakraborty S, Padmavathy N, Kulkarni GU (2014) Large area solution processed transparent conducting electrode based on highly interconnected Cu wire network. J Mater Chem C 2:2089–2094

[33] Gupta R, Rao KDM, Srivastava K, Kumar A, Kiruthika S, Kulkarni GU (2014) Spray coating of crack templates for the fabrication of transparent conductors and heaters on flat and curved surfaces. ACS Appl Mater Interfaces 6:13688–13696

[34] Voronin AS, Ivanchenko FS, Simunin MM, Shiverskiy AV, Aleksandrovsky AS, Nemtsev IV, Fadeev YV, Karpova DV, Khartov SV (2016) High performance hybrid rGO/Ag quasi-periodic mesh transparent electrodes for flexible electrochromic devices. Appl Surf Sci 364:931–937

[35] Tokuno T, Nogi M, Jiu JT, Sugahara T, Suganuma K (2012) Transparent electrodes fabricated via the self-assembly of silver nanowires using a bubble template. Langmuir 28:9298–9302

[36] Guo CF, Sun TY, Liu QH, Suo ZG, Ren ZF (2014) Highly stretchable and transparent nanomesh electrodes made by grain boundary lithography. Nat Commun 5:3121

[37] Zhu JF, Zhu XD, Hoekstra R, Li L, Xiu FX, Xue M, Zeng BQ, Wang KL (2012) Metallic nanomesh electrodes with controllable optical properties for organic solar cells. Appl Phys Lett 100:143109

[38] Gao TC, Wang BM, Ding B, Lee JK, Leu PW (2014) Uniform and ordered copper nanomeshes by microsphere lithography for transparent electrodes. Nano Lett 14:2105–2110

[39] Han Y, Lin J, Liu YX, Fu H, Ma Y, Jin P, Tan JB (2016) Crackle template based metallic mesh with highly homogeneous light transmission for high-performance transparent EMI shielding. Sci Rep 6:25601

[40] Zoski CG (2007) Handbook of electrochemistry. Elsevier, p 934

[41] Voronin AS, Simunin MM, Fadeev YV, Ivanchenko FS, Karpova DV, Tambasov IA, Khartov SV (2019) Technological basis of the formation of micromesh transparent electrodes by means of a self-organized template and the study of their properties. Tech Phys Lett 45:366–369

[42] Kiruthika S, Rao KDM, Kumar A, Gupta R, Kulkarni GU (2014) Metal wire network based transparent conducting electrodes fabricated using interconnected crackled layer as template. Mater Res Express 1:026301

[43] Periodic Table of Elements and X-ray Energies, https://www.bruker.com/products/x-ray-diffraction-and-elemental-analysis.

[44] Lee HB, Jin WY, Ovhal MM, Kumar N, Kang JW (2019) Flexible transparent conducting electrodes based on metal meshes for organic optoelectronic device applications: a review. J Mater Chem C 7:1087–1110

[45] Kim DH, Park MR, Lee GH (2006) Preparation of high quality ITO films on a plastic substrate using RF magnetron sputtering. Surf Coat Tech 201:927–931

[46] Song JZ, Kulinich SA, Li JH, Liu YL, Zeng HB (2015) A general one-pot strategy for the synthesis of high-performance transparent-conducting-oxide nanocrystal inks for all-solution-processed devices. Angew Chem Int Edit 54:462–466

[47] Hecht DS, Heintz AM, Lee R, Hu LB, Moore B, Cucksey C, Risser S (2011) High conductivity transparent carbon nanotube films deposited from superacid. Nanotechnology 22:075201

[48] Kaskela A, Nasibulin AG, Timmermans MY, Aitchison B, Papadimitratos A, Tian Y, Zhu Z, Jiang H, Brown DP, Zakhidov A, Kauppinen EI (2010) Aerosol-synthesized SWCNT networks with tunable conductivity and transparency by a dry transfer technique. Nano Lett 10:4349–4355

[49] Tsapenko AP, Goldt AE, Shulga E, Popov ZI, Maslakov KI, Anisimov AS, Sorokin PB, Nasibulin AG (2018) Highly conductive and transparent films of HAuCl$_4$-doped single-walled carbon nanotubes for flexible applications. Carbon 130:448–457

[50] Bae S, Kim H, Lee Y, Xu XF, Park JS, Zheng Y, Balakrishnan J, Lei T, Kim HR, Song YI, Kim YJ, Kim KS, Ozyilmaz B, Ahn JH, Hong BH, Iijima S (2010) Roll-to-roll production of 30-inch graphene films for transparent electrodes. Nat Nanotechnol 5:574–578

[51] Lee SJ, Kim YH, Kim JK, Baik H, Park JH, Lee J, Nam J, Park JH, Lee TW, Yi GR, Cho JH (2014) A roll-to-roll welding process for planarized silver nanowire electrodes. Nanoscale 6:11828–11834

[52] Ye SR, Rathmell AR, Stewart IE, Ha YC, Wilson AR, Chen ZF, Wiley BJ (2014) A rapid synthesis of high aspect ratio copper nanowires for high-performance transparent conducting films. Chem Commun 50:2562–2564

[53] Kim HJ, Kim Y, Jeong JH, Choi JH, Lee J, Choi DG (2015) A cupronickel-based micromesh film for use as a high-performance and low-voltage transparent heater. J Mater Chem A 3:16621–16626

[54] Vishwanath SK, Kim DG, Kim J (2014) Electromagnetic interference shielding effectiveness of invisible metal-mesh

prepared by electrohydrodynamic jet printing. Japanese J Appl Phys 53: 05HB11.

[55] Bonninghoff N, Chu JP, Chang CW, Mehretie M, Lai BZ (2018) Preparation and characterization of micron-scale molybdenum metal mesh electrodes. Surf Coat Tech 349:224–232

[56] Wu H, Kong DS, Ruan ZC, Hsu PC, Wang S, Yu ZF, Carney TJ, Hu LB, Fan SH, Cui Y (2013) A transparent electrode based on a metal nanotrough network. Nat Nanotechnol 8:421–425

[57] Kim MH, Joh H, Hong SH, Oh SJ (2019) Coupled Ag nanocrystal-based transparent mesh electrodes for transparent and flexible electro-magnetic interference shielding films. Curr Appl Phys 19:8–13

[58] Rao KDM, Kulkarni GU (2014) A highly crystalline single Au wire network as a high temperature transparent heater. Nanoscale 6:5645–5651

[59] Peng Q, Li SR, Han B, Rong QK, Lu XB, Wang QM, Zeng M, Zhou GF, Liu JM, Kempa K, Gao JW (2016) Colossal figure of merit in transparent-conducting metallic ribbon networks. Adv Mater Technol 1:1600095

[60] Tran DP, Lu HI, Lin CK (2015) Effects of cyclic deformation on conductive characteristics of indium tin oxide thin film on polyethylene terephthalate substrate. Surf & Coat Tech 283:298–310

[61] Park JW, Kim G, Lee SH, Kim EH, Lee GH (2010) The effect of film microstructures on cracking of transparent conductive oxide (TCO) coatings on polymer substrates. Surf Coat Tech 205:915–921

[62] Ahn S, Choe A, Park J, Kim H, Son JG, Lee SS, Park M, Ko H (2015) Directed self-assembly of rhombic carbon nanotube nanomesh films for transparent and stretchable electrodes. J Mater Chem C 3:2319–2325

[63] Lee P, Lee J, Lee H, Yeo J, Hong S, Nam KH, Lee D, Lee SS, Ko SH (2012) Highly stretchable and highly conductive metal electrode by very long metal nanowire percolation network. Adv Mater 24:3326–3332

[64] An BW, Gwak EJ, Kim K, Kim YC, Jang J, Kim JY, Park JU (2016) Stretchable, Transparent electrodes as wearable heaters using nanotrough networks of metallic glasses with superior mechanical properties and thermal stability. Nano Lett 16:471–478

[65] Zhang CP, Khan A, Cai JX, Liang CW, Liu YJ, Deng JH, Huang SY, Li GX, Li WD (2018) Stretchable transparent electrodes with solution-processed regular metal mesh for an electroluminescent light-emitting film. ACS Appl Mater Interfaces 10:21009–21017

[66] Khan A, Lee S, Jang T, Xiong Z, Zhang CP, Tang JY, Guo LJ, Li WD (2016) High-Performance flexible transparent electrode with an embedded metal mesh fabricated by cost-effective solution process. Small 12:3021–3030

[67] Zhou Y, Azumi R, Shimada S (2019) A highly durable, stretchable, transparent and conductive carbon nanotube–polymeric acid hybrid film. Nanoscale 11:3804–3813

[68] Jiang S, Hou PX, Chen ML, Wang BW, Sun DM, Tang DM, Jin Q, Guo QX, Zhang DD, Du JH, Tai KP, Tan J, Kauppinen EI, Liu C, Cheng HM (2018) Ultrahigh-performance transparent conductive films of carbon-welded isolated single-wall carbon nanotubes. Sci Adv 4:9264

[69] Gunes F, Shin HJ, Biswas C, Han GH, Kim ES, Chae SJ, Choi JY, Lee YH (2010) Layer-by-layer doping of few-layer graphene film. ACS Nano 4:4595–4600

[70] Qiu TF, Luo B, Liang MH, Ning J, Wang B, Li XL, Zhi LJ (2015) Hydrogen reduced graphene oxide/metal grid hybrid film: towards high performance transparent conductive electrode for flexible electrochromic devices. Carbon 81:232–238

[71] Seo KW, Noh YJ, Na SI, Kim HK (2016) Random mesh-like Ag networks prepared via self-assembled Ag nanoparticles for ITO-free flexible organic solar cells. Solar Energy Mater Solar Cells 155:51–59

[72] Geetha S, Kumar KKS, Rao CRK, Vijayan M, Trivedi DC (2009) EMI shielding: methods and materials-a review. J Appl Polym Sci 112:2073–2086

[73] Yang YL, Gupta MC (2005) Novel carbon nanotube-polystyrene foam composites for electromagnetic interference shielding. Nano Lett 5:2131–2134

[74] Shukla V (2019) Review of electromagnetic interference shielding materials fabricated by iron ingredients. Nanoscale Adv 1:1640–1671

[75] Han Y, Liu YX, Han L, Lin J, Jin P (2017) High-performance hierarchical graphene/metal-mesh film for optically transparent electromagnetic interference shielding. Carbon 115:34–42

[76] Liu YM, Tan JB (2013) Frequency dependent model of sheet resistance and effect analysis on shielding effectiveness of transparent conductive mesh coatings. Prog Electromagn Res 140:353–368

[77] Maniyara RA, Mkhitaryan VK, Chen TL, Ghosh DS, Pruneri V (2016) An antireflection transparent conductor with ultralow optical loss (<2 %) and electrical resistance (<6 Ω sq−1). Nat Commun 7:13771

[78] Lu ZG, Ma LM, Tan JB, Wang HY, Ding XM (2016) Transparent multi-layer graphene/polyethylene terephthalate structures with excellent microwave absorption and electromagnetic interference shielding performance. Nanoscale 8:16684–16693

[79] Kim DH, Kim Y, Kim JW (2016) Transparent and flexible film for shielding electromagnetic interference. Mater Design 89:703–707

[80] Shen S, Chen SY, Zhang DY, Liu YH (2018) High-performance composite Ag-Ni mesh based flexible transparent conductive film as multifunctional devices. Opt Express 26:27545–27554